Pushing the detection of cation nonstoichiometry to the limit

Editors' Suggestion

Pushing the detection of cation nonstoichiometry to the limit

Michele Riva,[1,*] Giada Franceschi,[1] Qiyang Lu,[2] Michael Schmid,[1] Bilge Yildiz,[1,2] and Ulrike Diebold[1]

[1]*Institute of Applied Physics, TU Wien, Wiedner Hauptstraße 8-10/E134, 1040 Wien, Austria*

[2]*Laboratory for Electrochemical Interfaces, Departments of Nuclear Science and Engineering, and Materials Science and Engineering, Massachusetts Institute of Technology, 77 Massachusetts Avenue, Cambridge, Massachusetts 02139, USA*

(Received 25 November 2018; published 25 April 2019)

Nanoscale complex-oxide thin films prepared by well-established growth techniques, such as pulsed-laser deposition or molecular-beam epitaxy, often exhibit compositions that deviate from the ideal stoichiometry. Even small variations in composition can lead to substantial changes in the technologically relevant electronic, magnetic, and optical properties of these materials. To assess the reasons behind this variability, and ultimately to allow tuning the properties of oxide films with precise control of the deposition parameters, high-resolution detection of the nonstoichiometry introduced during growth is needed. The resolution of current techniques, such as x-ray diffraction, fluorescence, or spectroscopy, is limited to estimating composition differences in the percent level, which is often insufficient for electronic-device quality. We develop an unconventional approach based on scanning tunneling microscopy for enabling the determination of cation imbalance introduced in thin films with exceptionally small detection limit. We take advantage of the well-controlled surface reconstructions on $SrTiO_3$(110), and use the established relation between those reconstructions and the surface composition to assess the cation excess deposited in pulsed-laser grown $SrTiO_3$(110) films. We demonstrate that a $<0.1\%$ change in cation nonstoichiometry is detectable by our approach. Furthermore, we show that, for thin films that accommodate all the nonstoichiometry at the surface, this method has no fundamental detection limit.

DOI: 10.1103/PhysRevMaterials.3.043802

I. INTRODUCTION

Transition-metal oxides display a rich manifold of phenomena taking place in their bulk, on their surfaces, and at their interfaces, which are driven directly by their local structure and/or by the nonstoichiometry of their composition. In particular, oxide semiconductors, such as $SrTiO_3$, are gaining increasing interest for use in electronic devices [1–3], especially in the form of nanoscale thin films. Recent advances in the synthesis techniques for such oxide films have stimulated the investigation of novel electronic [4–7], magnetic [8–10], ferroic [11], and ionic properties [12–15], enabled by the fabrication of multilayers, superlattices, and specialized interfaces [16–19]. Many of these properties strongly depend on stoichiometry: For example, a 1 at.% cationic composition deviation in $SrTiO_3$ can cause a variation in the carrier concentration of the order of 10^{20} cm^{-3} [20]. For this reason, strict control over film stoichiometry is essential. Compared to bulk crystals, however, it is generally much more difficult to accurately tune the composition in films of multielement complex oxides, such as $SrTiO_3$ [20–22]. For example, although pulsed-laser deposition (PLD) is taken as a technique to readily produce thin films with properties similar to the corresponding bulk material, small changes in deposition conditions, such as laser fluence or gas pressure, can lead to pronounced deviations in composition. Nonoptimal PLD growth conditions for homoepitaxial $SrTiO_3$ films result in significant cation nonstoichiometry [20,22,23], extended lattice constants [20,21,23], and can even cause $SrTiO_3$ films to become ferroelectric at room temperature [24,25].

The customary tools to characterize film stoichiometry include *ex situ* x-ray fluorescence (XRF), energy dispersive x-ray (EDS), or electron energy-loss spectroscopies (EELS) in a transmission electron microscope, x-ray photoelectron spectroscopy (XPS), Rutherford backscattering spectroscopy (RBS), and x-ray diffraction (XRD). XRF, EDS, EELS, and XPS directly measure compositions and are characterized by accuracies in quantifying the major elements of the order of a few percent [26]. RBS is capable of sensitivities as low as 0.5% on elemental ratios [26], but relies on appropriate modeling of the measured spectra. XRD, instead, measures the film lattice parameter, which is indirectly related to the stoichiometry of the compound [20,27,28]. For example, for $SrTiO_3$, both Ti and Sr excess give rise to an expansion of the lattice parameter relative to the stoichiometric value of 3.905 Å [20,27,29,30]. XRD is therefore limited to deviations from stoichiometry that are sufficiently large to produce detectable peak shifts. Furthermore, extended defects in the lattice, such as dislocations and grain boundaries, also lead to changes in the XRD patterns [31], to the extent that films grown by molecular-beam epitaxy (MBE) exhibit smaller lattice expansions with respect to PLD- or sputter-deposited ones at comparable deviations from the optimal stoichiometry [27]. As a result, significant uncertainties exist in establishing a universal relation between nonstoichiometry and lattice expansion. The resolution of these standard characterization techniques in measuring nonstoichiometry is significantly worse than the 0.1% (or better) detection limit that is required for oxide films suitable for electronic devices [32,33]. Such a

*Corresponding author: riva@iap.tuwien.ac.at

high sensitivity can be achieved with tools that exploit structural features that greatly depend on cation composition. In $SrTiO_3$, for example, it is now established that the Sr/Ti ratio present at the surface strongly affects the surface structure [34–38]. Recent reports have used reconstructions, observed by reflection high-energy electron diffraction (RHEED), as a sensitive measure of $SrTiO_3$ film stoichiometry [33,39], revealing that $SrTiO_3(001)$ homoepitaxial films exhibit significant changes in their surface reconstructions upon varying the growth parameters, even within the optimum growth window previously established by XRD [33]. This indicates that detection of such changes of the surface structure serves as a more sensitive tool to optimize film stoichiometry than XRD alone.

While electron diffraction readily provides qualitative insights in the change of surface structure, significant efforts are required for quantitative derivation of the atomic structure of surfaces and the fractional presence of reconstructions [40]. On the other hand, high-resolution scanning probe techniques, such as scanning tunneling microscopy (STM), provide unique resolution and direct quantitative characterization of the surface atomic structure. We propose the use of STM as a novel method for the detection of the cation imbalance deposited in thin films, and demonstrate our approach for deducing the cation excess introduced in homoepitaxial $SrTiO_3(110)$ films grown by PLD with an unprecedented small detection limit, i.e., order of 0.1% of the ideal Sr/Ti ratio. Central to our study of the $SrTiO_3(110)$ surface is the surface phase diagram established by Wang and co-workers [41], which describes the dependence of several surface reconstructions of $SrTiO_3(110)$ on the near-surface Sr/Ti ratio. Importantly, we note that, for the case of oxide films in which the nonstoichiometry is largely accommodated at the surface, as it is the case for $SrTiO_3(110)$, this approach has no lower detection limit for the deposited cation excess.

II. APPROACH

To enable the use of STM as a successful means to assess the cation imbalance introduced in thin films, it is first crucial to establish a quantitative relationship between surface composition and structure. Such a relation between the composition of a surface and its structure has been reported for several complex materials, including $LaAlO_3(110)$ [42], $LiNbO_3(0001)$ [43], $BaTiO_3(001)$ [44], $PbTiO_3(001)$ [45], and (001)-oriented [37,46], (110)-oriented [35,41], and (111)-oriented [47–49] $SrTiO_3$. We choose to illustrate the principles of our method on $SrTiO_3(110)$, as it is especially well established, both experimentally and theoretically, how its surface reconstructions are controlled by tuning the surface composition.

Along the [110] direction, $SrTiO_3$ is composed of alternating $(SrTiO)^{4+}$ and $(O_2)^{4-}$ planes, making this termination susceptible for the polar catastrophe, and intrinsically unstable in its bulk-terminated form [50]. Compensation of the diverging electrostatic energy is accomplished by introducing reconstructed TiO_x-rich layers bearing a formal $2e^-$ charge per bulk unit cell. Thanks to their origin in the polarity compensation, these reconstructed layers are exceptionally stable [51]. Monophase-reconstructed surfaces can be prepared by carefully adjusting the surface stoichiometry via Ar^+ sputtering or deposition of precisely defined Sr or Ti coverages, followed by high-temperature annealing in oxygen atmosphere [39,41]. The established relation between the relative changes in the surface Sr and Ti content and the surface reconstructions is illustrated in the surface phase diagram of $SrTiO_3(110)$ in Fig. 1. The (6×1), (5×1), (4×1), (2×4), (6×4), and (2×5) reconstructions are shown, as confirmed by STM and low-energy electron diffraction (LEED). Each of these surface reconstructions is enriched in Ti as compared to the bulk of $SrTiO_3$, and is composed of a combination of tetrahedrally and octahedrally coordinated TiO_x units, additionally including a few Sr atoms [34,35,52,53]. While the TiO_x enrichment is required to compensate for the polar nature of the $SrTiO_3(110)$ surface, each of the structures in Fig. 1 has a slightly different composition: Structures on the left of Fig. 1 are characterized by a smaller Ti enrichment than those on the right. Each surface structure represents a thermodynamic equilibrium phase, as determined by the cation chemical potentials, and can therefore be reversibly and reproducibly prepared by tuning the near-surface stoichiometry. This is achieved by deposition of small amounts of Sr or Ti (followed by high-temperature annealing in O_2 ambient) via, e.g., MBE [41] or PLD [51], as indicated in the bottom part of Fig. 1 in units of monolayers (ML). In this context, 1 ML corresponds to the number of Sr (or Ti) sites in a $(SrTiO)^{4+}$ plane of $SrTiO_3(110)$, i.e., 4.64×10^{14} at./cm^2 [32]. The determination of the Ti and Sr doses in Fig. 1 for the (6×1)-, (5×1)-, (4×1)-, (2×4)-, and (6×4)-reconstructed $SrTiO_3(110)$ surfaces has been obtained by Wang and co-workers by depositing the pure metals after careful calibration of the corresponding effusion cells [32,41]. To this aim, the authors optimized the temperatures of the sources to achieve exactly stoichiometric codeposition of Sr and Ti, as determined by RHEED. No calibration of the Ti dose needed to obtain (2×5)-reconstructed samples has been provided by these authors. We derived this dose in Fig. 1 by scaling the PLD-deposited TiO_2 amount necessary to move from (4×1) to (2×5) to the corresponding dose that allows switching between (5×1) and (4×1).

Based on the surface phase diagram in Fig. 1, it is possible to derive the stoichiometry of a monophase surface with respect to the one of an arbitrarily chosen reference structure. In fact, we show in the Supplemental Material, Sec. S I [54], that a one-to-one relation exists between the relative doses in Fig. 1 and the difference in the model compositions of the corresponding reconstructions. Thus, for example, referring the (4×1) reconstruction to the (5×1), one obtains that the former has $(0.55 - 0.4) \times (4.64 \times 10^{14}$ at./cm$^2) = 6.96 \times 10^{13}$ at./cm^2 Ti atoms more than the latter, or $(1.5 - 1.35) \times (4.64 \times 10^{14}$ at./cm$^2) = 6.96 \times 10^{13}$ at./cm^2 Sr atoms less.

The surface phase diagram in Fig. 1 allows the definition of the (relative) stoichiometry of the surface of a multiphase $SrTiO_3(110)$ sample. In case such a surface is composed of $i = 1, \ldots, k$ reconstructions with fractional coverages θ_i, its (relative) stoichiometry can be expressed as

$$S = \sum_{i=1}^{k} \theta_i (s_i - s_R) = \left(\sum_i \theta_i s_i \right) - s_R, \qquad (1)$$

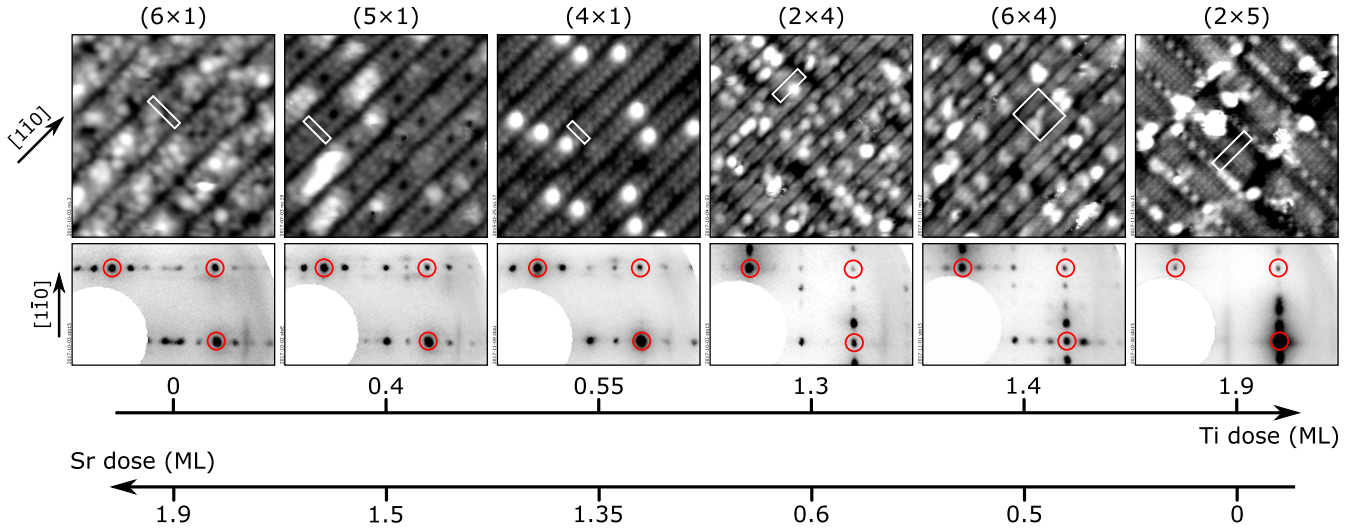

FIG. 1. Surface phase diagram of $SrTiO_3(110)$ showing selected reconstructions with different periodicities and their appearance in both STM images (top row; 12×12 nm^2 each) and LEED (bottom row; 90 eV, one quadrant shown with inverted gray scale). The reconstructed unit cells are outlined in white in each STM image. In each LEED pattern, the bulk-derived diffracted beams are highlighted with red circles. Each of the surface structures can be reversibly and reproducibly prepared by tuning the local surface stoichiometry. This can be achieved by deposition of small amounts of Sr or Ti via MBE or PLD (followed by high-temperature annealing in O_2 ambient), as indicated in the bottom part. As described in Sec. III, in this work Sr was deposited via a MBE Knudsen cell, while we used a TiO_2 PLD target as a Ti source. The surface phase diagram relates $SrTiO_3(110)$ reconstructions to one another and to their relative near-surface cation composition. The absolute compositions of (4×1) and (5×1) reconstructions are given in the Supplemental Material, Sec. S I [54].

where s_i and s_R correspond to the stoichiometry of a monophase surface with reconstruction i, and the one of a chosen reference structure, respectively. These quantities correspond to the cation doses reported in the surface phase diagram of Fig. 1.

Equation (1) allows direct comparison of the stoichiometry of any two $SrTiO_3(110)$ surfaces A, B in the form

$$\Delta S_{A,B} = S_B - S_A = \sum_i \left(\theta_i^B - \theta_i^A\right) s_i, \tag{2}$$

where the contribution of the (common) reference structure cancels out. It should be noted that A and B in Eq. (2) are entirely generic surfaces. Therefore, this relation can be used to compare the surface stoichiometry of a $SrTiO_3(110)$ film to the one of its corresponding substrate, as well as to compare the relative surface stoichiometry of two deposited films, or the change in the surface stoichiometry of a film as a result of post-growth treatments. It should be emphasized that Eqs. (1) and (2) describe only the stoichiometry of the very surface: Conclusions concerning the stoichiometry of the bulk underneath require to establish an appropriate relation between the stoichiometry of the surface and the one of the bulk itself. Such a relation is derived in Sec. II A for the growth of nonstoichiometric films, while in the Supplemental Material, Sec. S IV [54], we present some generalized models. Based on such models, we show in Sec. IV that Eq. (2) allows us to experimentally quantify the total nonstoichiometry of the deposited films with extremely high sensitivity.

A simplified version of Eq. (2) can be used when the same two reconstructions, at equilibrium with one another, are present on surfaces A and B (with different fractional coverages). In this case, the surface stoichiometry change can be calculated as

$$\Delta S_{A,B} = \Delta\theta_1^{B,A} \Delta s_{1,2}, \tag{3}$$

where $\Delta\theta_1^{B,A} = \theta_1^B - \theta_1^A$ is the difference in the coverage of the first reconstruction on the two surfaces, while $\Delta s_{1,2} = s_1 - s_2$. Notably, this situation does not require a complete quantitative knowledge of the surface phase diagram: only the dose $\Delta s_{1,2}$ to switch between the adjacent reconstructions of interest is needed.

A. Deposition of nonstoichiometric films

For the sake of simplicity, one can exemplify the evolution of the surface stoichiometry during the deposition of nonstoichiometric material on a stoichiometric substrate as follows. Assume that the deposited flux is characterized by a constant nonstoichiometry, such that a total excess x of one of the cations is introduced during the growth of every layer. This hypothesis is reasonably well verified in case the sticking coefficients of the deposited species do not change appreciably during growth or, equivalently, when the change in surface structure is small enough to neglect such differences in sticking probability. We assume that a fraction x_s of this cation excess floats at the surface during growth (modifying the surface reconstruction as discussed above), while the remaining cation excess $x_{b,f} = x - x_s$ remains stationary in the deposited layer (e.g., for kinetic reasons) and thus modifies the composition of the bulk of the film. Both contributions will affect the change in surface structure and, consequently, the evolution of the surface stoichiometry according to Eq. (2). Specifically, during the growth of each atomic layer, a cation excess $x = x_s + x_{b,f}$ is introduced in the surface layer. After the growth of the first atomic layer, the surface stoichiometry

changes, with respect to that of the substrate S_{sub}, as

$$\Delta S(1) = S(1) - S_{sub} = x = x_s + x_{b,f}.$$

Upon growth of the second layer, a cation excess $x_{b,f}$ is left behind in the subsurface layer, while x_s is transferred to the newly deposited layer. This quantity adds to the excess x introduced directly from the deposition, so that

$$\Delta S(2) = S(2) - S_{sub} = x_s + x = 2x_s + x_{b,f}.$$

Simple iteration of this reasoning leads to the expression for the change of surface stoichiometry (with respect to that of the substrate) upon growth of n layers:

$$\Delta S(n) = nx_s + x_{b,f}. \tag{4}$$

Therefore, Eqs. (2) and (4) allow to relate the change in the surface stoichiometry, accessible by STM measurements, to the excess number of cations incorporated both into the surface and in the bulk of the growing film.

According to the model in Eq. (4), two limiting conditions can be distinguished. On the one hand, the whole cation excess can be incorporated into the bulk of the growing film, so that $x_s = 0$ in Eq. (4), and the film nonstoichiometry is directly reflected in the surface stoichiometry change, i.e.,

$$x = x_{b,f} + x_s = x_{b,f} = \Delta S(n). \tag{5}$$

In this case, the change of surface stoichiometry does not depend on the thickness of the film, and it is realized already after the growth of the first oxide layer, and the minimum detectable nonstoichiometry is limited by the experimental uncertainty in measuring ΔS.

The other limiting case of Eq. (4), instead, occurs when the surface accommodates the entire excess of cations, while the bulk grows nearly stoichiometric (i.e., $x_{b,f} = 0$). As it will be shown in Sec. IV, this is the case for our $SrTiO_3(110)$ films. In this condition, the measured change of the surface stoichiometry is proportional to the total excess x and to the film thickness n as

$$\Delta S(n) = nx_s + x_{b,f} = nx_s = nx,$$

so that the total excess x can be derived as

$$x = \Delta S(n)/n. \tag{6}$$

Importantly, Eq. (6) implies that arbitrarily small cation imbalances can be detected by growing appropriately thick films. In particular, if the same two reconstructions are present, at equilibrium with one another, on the substrate and on the film, the minimum detectable cation excess amounts to

$$x_{min} = \frac{\Delta\theta_{min}\Delta s_{1,2}}{n}, \tag{7}$$

as obtained from inserting Eq. (3) into Eq. (6). The quantity $\Delta\theta_{min}$ in Eq. (7) corresponds to the minimum detectable change of fractional coverage of one of the two reconstructions. The minimum film thickness required to obtain a desired detection limit x_{min} correspondingly amounts to

$$n^{1,2}_{min} = \frac{\Delta\theta_{min}\Delta s_{1,2}}{x_{min}}. \tag{8}$$

Thus, $n^{1,2}_{min}$ depends on the dose $\Delta s_{1,2}$ required to switch between the adjacent reconstructions, as well as on the experimental technique used, which defines $\Delta\theta_{min}$. We estimate that STM allows to discriminate a $\Delta\theta^{STM}_{min} = 0.05$ areal coverage change with reasonable statistical efforts, so that detection of a 0.1% cation imbalance is obtained for film thicknesses larger than

$$n^{1,2}_{min,\,STM} = 50\,\Delta s_{1,2}.$$

For example, during deposition on a mixed $(4\times1)/(5\times1)$ surface ($\Delta s_{1,2} = 0.15$ ML) the minimum film thickness required to obtain a 0.1% detection limit amounts to $n^{(4\times1),(5\times1)}_{min,\,STM} = 7.5$ ML; instead, if the same detection limit is desired during growth on $(4 \times 1)/(2 \times 4)$ ($\Delta s_{1,2} = 0.75$ ML), a minimum film thickness $n^{(4\times1),(2\times4)}_{min,\,STM} = 37.5$ ML is necessary.

We would like to mention that our approach is applicable for any experimental technique capable of accessing the structure of the material's surface, and is not restricted to scanning probe microscopies. In fact, the method boils down to the determination of the fractional coverages of each reconstruction present at the surface [Eq. (2)]. This can also be accomplished, for example, by quantitatively analyzing LEED or RHEED diffraction patterns. In this case, one should expect a larger $\Delta\theta_{min}$ than with STM and, consequently, an increased detection limit for similarly thick films [Eq. (7)].

III. EXPERIMENTAL METHODS

One-side polished, Nb-doped (0.5 wt.%) $SrTiO_3(110)$ single crystals (CrysTec GmbH) were treated *ex situ* by sonication in heated neutral detergent (3% Extran® MA02, 2×30 min) and ultrapure water (milli-Q^{TM}, 10 min), followed by boiling in milli-Q^{TM} water (7 min). This procedure is especially effective in removing contamination by polishing remains. The samples were then prepared in an ultrahigh vacuum setup [55] by repeated cycles of Ar^+-ion sputtering (1 keV, 5–10 μA, 10 min), and annealing in O_2 atmosphere (6×10^{-6} mbar, 1000°C, 1 h), until no contamination was detectable by XPS (SPECS Phoibos 100 analyzer, and Omicron nonmonochromatized dual-anode Mg/Al Kα x-ray source) and STM (SPECS Aarhus 150).

The surface of the samples was prepared to show a mixed $(4 \times 1)/(5 \times 1)$ reconstruction, as judged by LEED (Omicron SpectaLEED) and STM. This is achieved by tuning the stoichiometry of the surface, according to the phase diagram in Fig. 1. The corresponding amounts of Sr and Ti were deposited at room temperature on the sample surface, and subsequently post annealed in O_2 (6×10^{-6} mbar, 1000°C, 30 min). Sr was deposited by MBE from a Knudsen cell (Createc) held at 420°C, while Ti was grown by PLD from a preablated single-crystalline rutile TiO_2 target in 6×10^{-6} mbar O_2 (Coherent CompexPro 201 KrF laser, focused to 1.09 ± 0.04 mm^2 at the target surface, as measured on a polished, polycrystalline Cu target via optical microscopy; laser fluence 2.5 J/cm^2; repetition rate 1 Hz; target-substrate distance 55 mm).

$SrTiO_3$ homoepitaxial films were grown on these samples by PLD from Nb-doped (0.5 wt.%) single-crystalline $SrTiO_3$ targets (MaTeck and CrysTec) at 750°C in O_2 background (6×10^{-6} mbar), and post annealed for 10 min at the same conditions. The thickness

of the deposited films was measured by live monitoring the intensity of the specular spot of reflected electrons from RHEED (Staib Instruments Torr-RHEED, beam along the [001] direction) [55]. The PLD growth of both the small TiO_2 amounts and the $SrTiO_3$ films was performed as previously described [55]. Specifically, a fresh, newly polished area of the target was chosen each time, and preablated at the same conditions used later for the growth. The preablated area was scanned in the UV laser beam such as to hit each spot with at least 10 laser pulses (in total, including both preablation and growth, each spot on the target was hit a maximum of 48 times). During preablation, the sample was kept in an adjacent, separate chamber, to prevent deposition of unwanted species on the surface [55]. The laser fluences (1.6–2.6 J/cm^2) were always recalibrated 1–2 min before growth: pulse energies were measured (Coherent EnergyMax) via a through-chamber setup that automatically takes into account the transmission of the UV entrance window. All the growth experiments were carried out at 1-Hz repetition frequency.

After growth, the samples were transferred, without breaking vacuum, to the analysis chamber, where their surface structure and stoichiometry were characterized by STM, LEED, and XPS. All the uncertainties on the surface stoichiometry changes correspond to 99% confidence intervals, as derived from the evaluation of several STM images (see Sec. IV for details) and exclude possible uncertainties in the determination of the cation doses reported in the surface phase diagram of Fig. 1. These doses, however, are deemed to be accurate within a few percent (see Supplemental Material, Sec. S I, for details [54]).

IV. IMPLEMENTATION

Figure 2 compares the morphology and structure of an as-prepared $SrTiO_3$(110) substrate and of the corresponding ≈15-layers-thick (≈4.2 nm) homoepitaxial film grown on it by PLD, at 1.9 J/cm^2 fluence of the UV laser. On large-area STM images [Figs. 2(a) and 2(b)], both substrate and film show (20–300)-nm-large, atomically flat terraces, separated by single-layer or multilayer steps. The deposition was interrupted just after the completion of the 15th atomic layer, as can be noticed from the *in situ* RHEED intensity oscillations in Fig. 2(i). As a result, a few single-layer-high, atomically flat islands are visible on the terraces of the surface of the film in Fig. 2(b) [55]. Upon growth, the surface structure changes from predominantly (4 × 1) to mainly (5 × 1) reconstructed, as seen from the LEED patterns in Figs. 2(g) and 2(h). This corresponds to a change toward a more Sr-rich surface. Such a change is reflected in the atomic-scale STM images of Figs. 2(c) and 2(d), as well as in their Fourier transforms [Figs. 2(e) and 2(f)], whose intensity maxima closely mimic the corresponding LEED patterns. In Figs. 2(c) and 2(d), lines with (4 × 1) and (5 × 1) periodicities are highlighted for clarity in red and blue, respectively. The narrower (4 × 1)-reconstructed lines can also be distinguished by the regularly spaced, circular bright protrusions that have been identified as isolated Sr adatoms [53]. Lines with (5 × 1) periodicity, instead, are characterized by larger, irregularly shaped bright features, and by regularly spaced dark spots that correspond to antiphase domain boundaries [52].

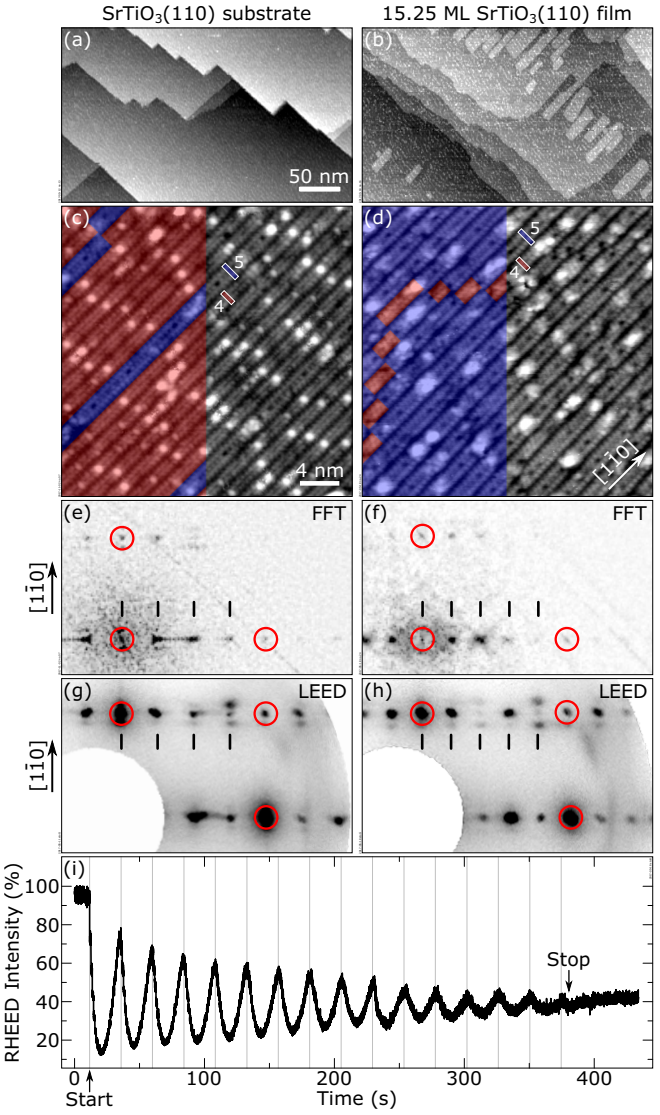

FIG. 2. Morphology [(a), (b) STM, 350 × 210 nm^2], and atomic-scale structure of (a), (c), (e), (g) an as-prepared $SrTiO_3$(110) substrate, and (b), (d), (f), (h) a 15.25-layers-thick homoepitaxial film grown on top of it (laser fluence 1.9 J/cm^2). (c), (d) STM images (30 × 30 nm^2), (e), (f) Fourier transforms (one quadrant, inverted gray scale), and (g), (h) LEED patterns (90 eV, inverted gray scale). In the left half of panels (c) and (d), lines exhibiting (4 × 1) and (5 × 1) periodicities are highlighted in red and blue, respectively, while the corresponding reconstructed unit cells are outlined in white. In panels (e) and (f), the origin of Fourier space (bottom left), as well as the first-order (1 × 1) periodicities are indicated with red circles. Vertical dashes highlight maxima corresponding to the reconstructed periodicities. In panels (g) and (h), bulk-derived (1 × 1) diffracted beams are marked with red circles, while the periodicity of reconstruction-related spots is marked by vertical dashes. Panel (i) shows the intensity of the specular RHEED spot during growth. Intensity maxima, with a periodicity of 24.2 s, are highlighted by vertical, gray lines. In total, 369 UV laser pulses were used for deposition.

As compared to the qualitative picture provided by LEED, STM allows a quantitative determination of the relative coverage of the two reconstructions by directly measuring the

fractional areas occupied by the two reconstructions. It should be noticed that, since (4 × 1) and (5 × 1) belong to the same family of homologous structures [35], lines with the two periodicities are usually interwoven, and do not phase separate into distinct domains. On several occasions [see, e.g., the (5 × 1) line in the top-left part of Fig. 2(c), and the (4 × 1) line in Fig. 2(d)] lines of one reconstruction can "jump" one (or multiple) lattice units along the [001] direction, so that the lines can appear fragmented. Nonetheless, each of them appears to continuously run on the surface along the $[1\bar{1}0]$ direction, so that the relative area coverage of each of the structures can be determined by counting the number of lines and scaling this number with the periodicity of the corresponding structure. For example, the relative coverage of (4 × 1)-reconstructed areas in a sample comprising (4 × 1) and (5 × 1) reconstructions can be calculated as

$$\theta_{4\times1} = \frac{4N_{4\times1}}{4N_{4\times1} + 5N_{5\times1}},$$

where $N_{4\times1/5\times1}$ are the number of (4 × 1) and (5 × 1) lines in an STM image. This coverage can be directly plugged into Eq. (2) to derive the change of surface stoichiometry, as described in Sec. II. To gain enough statistical significance, several STM images comparable to those in Figs. 2(c) and 2(d) were acquired at different spots on the sample, totaling 1000–2000 lines (typically this corresponds to acquiring 15–30 images of 70 × 70 nm^2 size). With this approach, we determine that 85.4 ± 3.5% of the surface of the substrate in Fig. 2(c) has a (4 × 1) reconstruction, while 14.6 ± 3.5% is (5 × 1) reconstructed. After growth of a 15.25-layers-thick film, 10.6 ± 1.4% of the surface of the sample retains the (4 × 1) reconstruction, while 89.4 ± 1.4% is (5 × 1). According to Eq. (2), this corresponds to a change in the surface stoichiometry upon growth of 0.1122 ± 0.0080 ML Sr.

In the limiting case where the nonstoichiometry of the deposited material is fully accommodated in the bulk of the film [Eq. (5)], and when, consequently, the change of the surface stoichiometry directly reflects the off stoichiometry of the bulk underneath, such a change in the surface stoichiometry would correspond to a $Sr_{1.1122\pm0.0080}TiO_x$ film composition. This should be clearly detectable by XPS, and should result in a severely expanded (Δc = 10–15 pm) out-of-plane lattice parameter in XRD [20]. However, our XPS measurements (see Supplemental Material, Sec. S II [54]) show that, within the error bars, the Sr 3*d*/Ti 2*p* intensity ratio does not change as a result of the film growth. Given that the inelastic mean-free path for these photoelectrons is approximately half the film thickness, the 0.4 ± 1.6% measured change sets a rough upper limit to the film off stoichiometry of ≈2%. Consistently, high-resolution XRD (see Supplemental Material, Sec. S IV [54]) shows only a single peak at the scattering angle 2Θ expected for $SrTiO_3$(110), and no additional features are visible at those angles where a 10-pm out-of-plane lattice expansion would be expected [56]. Therefore, neither XPS nor XRD can distinguish between the substrate and the homoepitaxial film in Fig. 2, while the stoichiometry difference at the surface is clearly observable by STM.

In the other limiting case, the surface is assumed to accommodate the whole cation excess, while the nonstoichiometry in the film bulk can be largely neglected. It should be mentioned that segregation of cation nonstoichiometry to the surface of growing films has been previously invoked to explain the lack of expanded lattice constants in XRD during the growth of $SrTiO_3$(001) thin films by PLD [57] and sputtering [58]. As discussed in the following, our experimental evidence supports that this scenario applies to our $SrTiO_3$(110) films, so that the excess $x = x_s$ of Sr atoms in the deposited flux can be evaluated from Eq. (6), and amounts to 0.74 ± 0.05%. Therefore, our method allows the detection of deposited cation excess well below 1%. The minimum detectable cation imbalance introduced during the growth of films with thickness comparable to those in Fig. 2 is determined by the 0.05% statistical uncertainty.

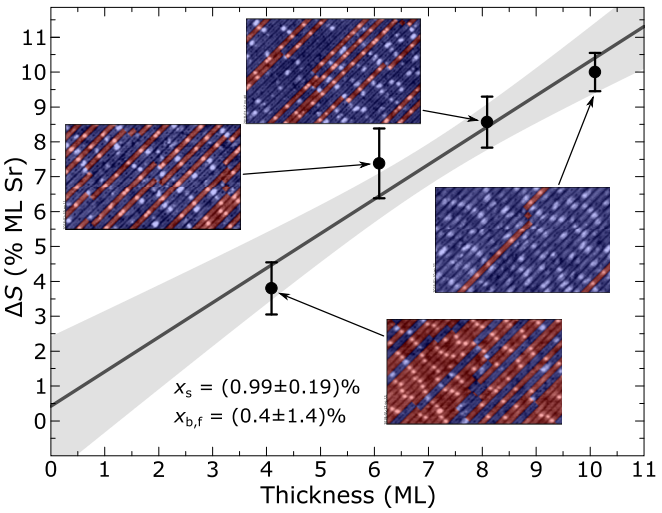

FIG. 3. Change of surface stoichiometry upon homoepitaxial growth of $SrTiO_3$(110) films of increasing thickness (laser fluence 1.7 J/cm^2), as derived from STM data. Error bars correspond to 99% confidence intervals, as derived from the statistical evaluation of STM images. Representative STM images (50 × 30 nm^2) are shown as insets. (4 × 1)- and (5 × 1)-reconstructed areas are highlighted in red and blue, respectively. The gray line represents a linear fit to the data, while the shaded area corresponds to the 70% confidence band of the fit. The slope (x_s) and intercept ($x_{b,f}$) of the linear fit are reported together with their standard errors.

In order to support our hypothesis that the excess deposited cations are largely accommodated at the surface, homoepitaxial $SrTiO_3$(110) films of varying thickness were deposited at 1.7 J/cm^2 laser fluence. Figure 3 reports the change of surface stoichiometry ΔS, quantitatively determined by STM, as a function of the thickness of the deposited film. It should be noted that each of the films was grown on the same substrate, after the surface had been reprepared to exhibit a fractional coverage of (4 × 1)-reconstructed areas ranging between 75% and 85%. As shown by the STM images in the insets of Fig. 3, the surface structure of the film progressively evolves from mixed (4 × 1)/(5 × 1)-reconstructed to an essentially pure (5 × 1) periodicity. Correspondingly, the change in surface stoichiometry ΔS linearly increases with the thickness of the deposited film, consistently with the model in Eq. (4). A linear fit to the data (gray line in Fig. 3) allows us to estimate the fractional excess of Sr atoms accommodated at

the surface (x_s) and distributed in the bulk ($x_{b,f}$), as the slope and intercept of the fitting line, respectively. Specifically, we find that a nonzero excess fraction $x_s = 0.99 \pm 0.19\%$ of Sr atoms accumulates at the surface of the growing film for each deposited layer. At the same time, there is no statistical evidence that the amount of excess Sr cations distributed in the bulk of the film ($x_{b,f} = 0.4 \pm 1.4\%$) is different from zero. An independent estimation of the total amount of cation excess in the bulk of the films is presented in the Supplemental Material (Sec. S IV B) [54]: the samples were annealed at elevated temperatures after deposition. This way, the cation nonstoichiometry possibly accumulated in the bulk of the film could segregate to the surface or get diluted into the substrate. Either case would cause a change of the surface composition and structure. We quantitatively determined the change of surface structure upon post annealing for a homoepitaxial $SrTiO_3(110)$ film, and estimated a maximum total amount of Sr excess in the bulk of $-0.10 \pm 0.08\%$. This supports the hypothesis that, under our experimental conditions, a negligible fraction of the deposited cation excess is incorporated in the bulk of the film. Most of the excess cations deposited accumulate at the surface during growth.

We hypothesize that this behavior is due to the large variety of reconstructions characteristic of the $SrTiO_3(110)$ surface that can effectively accommodate excess cations at smaller energetic cost [35] than by introducing bulk defects. In $SrTiO_3$, these bulk defects commonly consist either of antisite point defects or of {001}-oriented SrO planes [30]: the formation of antisite point defects requires significantly larger energy (1–4 eV/defect [59]) than modifying the surface reconstruction [$\lesssim$0.2 eV/(1 × 1) unit cell [35]], while Ruddlesden-Popper planes [0.5 eV per $SrTiO_3(001)$ unit cell [60]] would inevitably result in energetically expensive crystallographic defects at our (110)-oriented surface.

The difference in the energetics of bulk defects formation (>1 eV/defect [30,59–65]) and surface restructuring (a few fractions of an electronvolt per unit cell [46,49]) is not a specific property of our $SrTiO_3(110)$: restructuring of surfaces during growth will generally occur more favorably than introduction of bulk defects, provided that kinetics allows it. Specifically, we anticipate that segregation of the deposited cation imbalance should effectively occur under the following conditions:

(i) The material exhibits (at least two) surface-composition-driven reconstructions. This appears to be the case for a variety of complex oxide surfaces other than our $SrTiO_3(110)$ [37,42–49], and is likely true for other nonoxide materials.

(ii) The nonstoichiometry introduced during growth is small enough, such that surface restructuring allows its accommodation. Introduction of nonstoichiometric bulk defects [30,33] or precipitation of secondary phases is likely to occur if the deposited cation imbalance exceeds the largest excess that can be accommodated in the surface reconstructions. If this is the case, traditional techniques will be more suited.

(iii) The growth temperature and rate are chosen such that equilibration of the surface structures is appropriately established. The cation chemical potentials during deposition are uniquely determined by the combination of surface reconstructions, and are fixed in case only the same two reconstructions are present at all stages. This makes the inclusion of nonstoichiometric bulk defects unfavorable (see also Supplemental Material, Sec. S IV [54]).

When these conditions are met so that the deposited cation imbalance is largely accommodated at the surface, the prowess of our method can be fully exploited via Eq. (6). This should be possible for several materials other than our $SrTiO_3(110)$ surfaces.

V. CONCLUSIONS

In conclusion, we introduce an unconventional approach to quantitatively determine the cation excess deposited during the growth of complex-oxide thin films with exceptionally small detection limit, based on the characterization of their surface structure via scanning tunneling microscopy. The method relies on an established surface phase diagram that relates specific reconstructions to one another and to the corresponding difference in their near-surface cation stoichiometry; the phase diagram can be restricted to a minimum of two adjacent reconstructions, and can either be derived from the literature or determined in the same experimental setup.

We demonstrate the prowess of the method by determining the cation excess introduced in homoepitaxial $SrTiO_3(110)$ films grown by pulsed laser deposition in the same vacuum system, and argue that deposited cation imbalances deviating by less than 0.1% from the ideal bulk concentration can be readily detected. Furthermore, in cases where the cation excess is mainly accommodated at the surface, as we demonstrate for our $SrTiO_3(110)$ homoepitaxial thin films, this method does not suffer from the existence of a fundamental detection limit on the cation nonstoichiometry of the deposited flux.

The rise of semiconductor-based electronics has gone hand in hand with the technological advancements allowing to reproducibly prepare materials with exceptionally small defect concentrations. Similar control of defects and composition is the key to making all-oxide electronics a reality, allowing to fully exploit the multitude of functionalities of these fascinating materials. Precise tuning of the oxide composition, however, necessarily requires the development of reliable tools to detect cation nonstoichiometry with extreme sensitivity: our method pushes down this detection limit by at least one order of magnitude.

ACKNOWLEDGMENTS

This work was supported by the Austrian Science Fund FWF [SFB "Functional Oxide Surfaces and Interfaces" (FOXSI), Project F 45] and by the Vienna Science and Technology Fund WWTF (Project MoDeNa, No. MA16-005). G.F. acknowledges support from the TU-D doctoral college of the TU Wien. B.Y. also acknowledges the NSF CAREER Award of the National Science Foundation, Division of Materials Research, Ceramics Program, Grant No. 1055583, for partially supporting her sabbatical work at TU Wien. Q.L. and B.Y. acknowledge support of the U. S. National Science Foundation, Division of Materials Research through the Massachusetts Institute of Technology Materials Research Science and Engineering Center, Grant No. 1419807.

[1] W. Gao, M. Yao, and X. Yao, Achieving ultrahigh breakdown strength and energy storage performance through periodic interface modification in $SrTiO_3$ thin film, ACS Appl. Mater. Interfaces **10**, 28745 (2018).

[2] K. S. Takahashi, M. Gabay, D. Jaccard, K. Shibuya, T. Ohnishi, M. Lippmaa, and J. M. Triscone, Local switching of two-dimensional superconductivity using the ferroelectric field effect, Nature (London) **441**, 195 (2006).

[3] S. W. Zeng, X. M. Yin, T. S. Herng, K. Han, Z. Huang, L. C. Zhang, C. J. Li, W. X. Zhou, D. Y. Wan, P. Yang *et al.*, Oxygen Electromigration and Energy Band Reconstruction Induced by Electrolyte Field Effect at Oxide Interfaces, Phys. Rev. Lett. **121**, 146802 (2018).

[4] P. Schütz, D. Di Sante, L. Dudy, J. Gabel, M. Stübinger, M. Kamp, Y. Huang, M. Capone, M.-A. Husanu, V. N. Strocov *et al.*, Dimensionality-Driven Metal-Insulator Transition in Spin-Orbit-Coupled $SrIrO_3$, Phys. Rev. Lett. **119**, 256404 (2017).

[5] F. Gunkel, C. Bell, H. Inoue, B. Kim, A. G. Swartz, T. A. Merz, Y. Hikita, S. Harashima, H. K. Sato, M. Minohara *et al.*, Defect Control of Conventional and Anomalous Electron Transport at Complex Oxide Interfaces, Phys. Rev. X **6**, 031035 (2016).

[6] A. Chikina, F. Lechermann, M.-A. Husanu, M. Caputo, C. Cancellieri, X. Wang, T. Schmitt, M. Radovic, and V. N. Strocov, Orbital ordering of the mobile and localized electrons at oxygen-deficient $LaAlO_3/SrTiO_3$ interfaces, ACS Nano **12**, 7927 (2018).

[7] Z. Zhong and P. Hansmann, Band Alignment and Charge Transfer in Complex Oxide Interfaces, Phys. Rev. X **7**, 011023 (2017).

[8] B.-C. Huang, P. Yu, Y. H. Chu, C.-S. Chang, R. Ramesh, R. E. Dunin-Borkowski, P. Ebert, and Y.-P. Chiu, Atomically resolved electronic states and correlated magnetic order at termination engineered complex oxide heterointerfaces, ACS Nano **12**, 1089 (2018).

[9] H. Boschker and J. Mannhart, Quantum-matter heterostructures, Annu. Rev. Condens. Matter Phys. **8**, 145 (2017).

[10] F. Hellman, A. Hoffmann, Y. Tserkovnyak, G. S. D. Beach, E. E. Fullerton, C. Leighton, A. H. MacDonald, D. C. Ralph, D. A. Arena, H. A. Dürr *et al.*, Interface-induced phenomena in magnetism, Rev. Mod. Phys. **89**, 025006 (2017).

[11] F. Motti, G. Vinai, A. Petrov, B. A. Davidson, B. Gobaut, A. Filippetti, G. Rossi, G. Panaccione, and P. Torelli, Strain-induced magnetization control in an oxide multiferroic heterostructure, Phys. Rev. B **97**, 094423 (2018).

[12] W. Xue, G. Liu, Z. Zhong, Y. Dai, J. Shang, Y. Liu, H. Yang, X. Yi, H. Tan, L. Pan, S. Gao, J. Ding, X.-H. Xu, and R.-W. Li, A 1D vanadium dioxide nanochannel constructed via electric-field-induced ion transport and its superior metal-insulator transition, Adv. Mater. **29**, 1702162 (2017).

[13] D. A. Gilbert, A. J. Grutter, P. D. Murray, R. V. Chopdekar, A. M. Kane, A. L. Ionin, M. S. Lee, S. R. Spurgeon, B. J. Kirby, B. B. Maranville *et al.*, Ionic tuning of cobaltites at the nanoscale, Phys. Rev. Mater. **2**, 104402 (2018).

[14] E. Linn, R. Rosezin, C. Kügeler, and R. Waser, Complementary resistive switches for passive nanocrossbar memories, Nat. Mater. **9**, 403 (2010).

[15] J. J. Yang, D. B. Strukov, and D. R. Stewart, Memristive devices for computing, Nat. Nanotechnol. **8**, 13 (2013).

[16] S.-C. Lin, C.-T. Kuo, R. B. Comes, J. E. Rault, J.-P. Rueff, S. Nemšák, A. Taleb, J. B. Kortright, J. Meyer-Ilse, E. Gullikson *et al.*, Interface properties and built-in potential profile of a $LaCrO_3/SrTiO_3$ superlattice determined by standing-wave excited photoemission spectroscopy, Phys. Rev. B **98**, 165124 (2018).

[17] J. D. Hoffman, B. J. Kirby, J. Kwon, G. Fabbris, D. Meyers, J. W. Freeland, I. Martin, O. G. Heinonen, P. Steadman, H. Zhou *et al.*, Oscillatory Noncollinear Magnetism Induced by Interfacial Charge Transfer in Superlattices Composed of Metallic Oxides, Phys. Rev. X **6**, 041038 (2016).

[18] A. Ohtomo and H. Y. Hwang, A high-mobility electron gas at the $LaAlO_3/SrTiO_3$ heterointerface, Nature (London) **427**, 423 (2004).

[19] R. B. Comes, S. R. Spurgeon, S. M. Heald, D. M. Kepaptsoglou, L. Jones, P. V. Ong, M. E. Bowden, Q. M. Ramasse, P. V. Sushko, and S. A. Chambers, Interface-induced polarization in $SrTiO_3$-$LaCrO_3$ superlattices, Adv. Mater. Interfaces **3**, 1500779 (2016).

[20] T. Ohnishi, K. Shibuya, T. Yamamoto, and M. Lippmaa, Defects and transport in complex oxide thin films, J. Appl. Phys. **103**, 103703 (2008).

[21] K. Orsel, R. Groenen, B. Bastiaens, G. Koster, G. Rijnders, and K.-J. Boller, Influence of the oxidation state of $SrTiO_3$ plasmas for stoichiometric growth of pulsed laser deposition films identified by laser induced fluorescence, APL Mater. **3**, 106103 (2015).

[22] E. Breckenfeld, R. Wilson, J. Karthik, A. R. Damodaran, D. G. Cahill, and L. W. Martin, Effect of growth induced (non)stoichiometry on the structure, dielectric response, and thermal conductivity of $SrTiO_3$ thin films, Chem. Mater. **24**, 331 (2012).

[23] T. Ohnishi, M. Lippmaa, T. Yamamoto, S. Meguro, and H. Koinuma, Improved stoichiometry and misfit control in perovskite thin film formation at a critical fluence by pulsed laser deposition, Appl. Phys. Lett. **87**, 241919 (2005).

[24] F. Yang, Q. Zhang, Z. Yang, J. Gu, Y. Liang, W. Li, W. Wang, K. Jin, L. Gu, and J. Guo, Room-temperature ferroelectricity of $SrTiO_3$ films modulated by cation concentration, Appl. Phys. Lett. **107**, 082904 (2015).

[25] Y. S. Kim, D. J. Kim, T. H. Kim, T. W. Noh, J. S. Choi, B. H. Park, and J.-G. Yoon, Observation of room-temperature ferroelectricity in tetragonal strontium titanate thin films on $SrTiO_3$(001) substrates, Appl. Phys. Lett. **91**, 042908 (2007).

[26] A. Ojeda-G-P, M. Döbeli, and T. Lippert, Influence of plume properties on thin film composition in pulsed laser deposition, Adv. Mater. Interfaces **5**, 1701062 (2018).

[27] C. M. Brooks, L. F. Kourkoutis, T. Heeg, J. Schubert, D. A. Muller, and D. G. Schlom, Growth of homoepitaxial $SrTiO_3$ thin films by molecular-beam epitaxy, Appl. Phys. Lett. **94**, 162905 (2009).

[28] D. A. Freedman, D. Roundy, and T. A. Arias, Elastic effects of vacancies in strontium titanate: Short- and long-range strain fields, elastic dipole tensors, and chemical strain, Phys. Rev. B **80**, 064108 (2009).

[29] D. Fuchs, M. Adam, P. Schweiss, S. Gerhold, S. Schuppler, R. Schneider, and B. Obst, Structural properties of slightly off-stoichiometric homoepitaxial $SrTi_xO_{3-\delta}$ thin films, J. Appl. Phys. **88**, 1844 (2000).

[30] C. Xu, H. Du, A. J. H. van der Torren, J. Aarts, C.-L. Jia, and R. Dittmann, Formation mechanism of Ruddlesden-Popper-type antiphase boundaries during the kinetically limited growth of Sr rich $SrTiO_3$ thin films, Sci. Rep. **6**, 38296 (2016).

[31] A. I. Benediktovich, I. D. Feranchuk, and A. Ulyanenkov, X-ray dynamical diffraction from partly relaxed epitaxial structures, Phys. Rev. B **80**, 235315 (2009).

[32] Z. Wang, J. Feng, Y. Yang, Y. Yao, L. Gu, F. Yang, Q. Guo, and J. Guo, Cation stoichiometry optimization of $SrTiO_3(110)$ thin films with atomic precision in homogeneous molecular beam epitaxy, Appl. Phys. Lett. **100**, 051602 (2012).

[33] A. P. Kajdos and S. Stemmer, Surface reconstructions in molecular beam epitaxy of $SrTiO_3$, Appl. Phys. Lett. **105**, 191901 (2014).

[34] Z. Wang, A. Loon, A. Subramanian, S. Gerhold, E. McDermott, J. A. Enterkin, M. Hieckel, B. C. Russell, R. J. Green, A. Moewes *et al.*, Transition from reconstruction toward thin film on the (110) surface of strontium titanate, Nano Lett. **16**, 2407 (2016).

[35] J. A. Enterkin, A. K. Subramanian, B. C. Russell, M. R. Castell, K. R. Poeppelmeier, and L. D. Marks, A homologous series of structures on the surface of $SrTiO_3(110)$, Nat. Mater. **9**, 245 (2010).

[36] M. R. Castell, Scanning tunneling microscopy of reconstructions on the $SrTiO_3(001)$ surface, Surf. Sci. **505**, 1 (2002).

[37] S. Gerhold, Z. Wang, M. Schmid, and U. Diebold, Stoichiometry-driven switching between surface reconstructions on $SrTiO_3(001)$, Surf. Sci. **621**, L1 (2014).

[38] R. Shimizu, K. Iwaya, T. Ohsawa, S. Shiraki, T. Hasegawa, T. Hashizume, and T. Hitosugi, Atomic-scale visualization of initial growth of homoepitaxial $SrTiO_3$ thin film on an atomically ordered substrate, ACS Nano **5**, 7967 (2011).

[39] J. Feng, F. Yang, Z. Wang, Y. Yang, L. Gu, J. Zhang, and J. Guo, Growth of $SrTiO_3(110)$ film by oxide molecular beam epitaxy with feedback control, AIP Adv. **2**, 041407 (2012).

[40] R. Bliem, E. McDermott, P. Ferstl, M. Setvin, O. Gamba, J. Pavelec, M. A. Schneider, M. Schmid, U. Diebold, P. Blaha *et al.*, Subsurface cation vacancy stabilization of the magnetite (001) surface, Science **346**, 1215 (2014).

[41] Z. Wang, F. Yang, Z. Zhang, Y. Tang, J. Feng, K. Wu, Q. Guo, and J. Guo, Evolution of the surface structures on $SrTiO_3(110)$ tuned by Ti or Sr concentration, Phys. Rev. B **83**, 155453 (2011).

[42] D. Kienzle, P. Koirala, and L. D. Marks, Lanthanum aluminate (110) 3×1 surface reconstruction, Surf. Sci. **633**, 60 (2015).

[43] S. V. Levchenko and A. M. Rappe, Influence of Ferroelectric Polarization on the Equilibrium Stoichiometry of Lithium Niobate (0001) Surfaces, Phys. Rev. Lett. **100**, 256101 (2008).

[44] A. M. Kolpak, D. Li, R. Shao, A. M. Rappe, and D. A. Bonnell, Evolution of the Structure and Thermodynamic Stability of the $BaTiO_3(001)$ Surface, Phys. Rev. Lett. **101**, 036102 (2008).

[45] W. A. Saidi, J. M. P. Martirez, and A. M. Rappe, Strong reciprocal interaction between polarization and surface stoichiometry in oxide ferroelectrics, Nano Lett. **14**, 6711 (2014).

[46] S. Cook and L. D. Marks, *Ab initio* predictions of double-layer TiO_2-terminated $SrTiO_3(001)$ surface reconstructions, J. Phys. Chem. C **122**, 21991 (2018).

[47] F. Yang, Y. Liang, L.-X. Liu, Q. Zhu, W.-H. Wang, X.-T. Zhu, and J.-D. Guo, Controlled growth of complex polar oxide films with atomically precise molecular beam epitaxy, Front. Phys. **13**, 136802 (2018).

[48] B. C. Russell and M. R. Castell, Surface of sputtered and annealed polar $SrTiO_3(111)$: TiO_x-rich $(n \times n)$ reconstructions, J. Phys. Chem. C **112**, 6538 (2008).

[49] T. K. Andersen, S. Wang, M. R. Castell, D. D. Fong, and L. D. Marks, Single-layer TiO_x reconstructions on $SrTiO_3(111)$: $(\sqrt{7} \times \sqrt{7})$R19.1°, $(\sqrt{13} \times \sqrt{13})$R13.9°, and related structures, Surf. Sci. **675**, 36 (2018).

[50] C. Noguera and J. Goniakowski, Polarity in oxide nano-objects, Chem. Rev. **113**, 4073 (2013).

[51] M. Riva, M. Kubicek, X. Hao, G. Franceschi, S. Gerhold, M. Schmid, H. Hutter, J. Fleig, C. Franchini, B. Yildiz, and U. Diebold, Influence of surface atomic structure demonstrated on oxygen incorporation mechanism at a model perovskite oxide, Nat. Commun. **9**, 3710 (2018).

[52] Z. Wang, X. Hao, S. Gerhold, M. Schmid, C. Franchini, and U. Diebold, Vacancy clusters at domain boundaries and band bending at the $SrTiO_3(110)$ surface, Phys. Rev. B **90**, 035436 (2014).

[53] Z. Wang, F. Li, S. Meng, J. Zhang, E. W. Plummer, U. Diebold, and J. Guo, Strain-Induced Defect Superstructure on the $SrTiO_3(110)$ Surface, Phys. Rev. Lett. **111**, 056101 (2013).

[54] See Supplemental Material at http://link.aps.org/supplemental/10.1103/PhysRevMaterials.3.043802 for Sec. S I: comparison of experimental coverages and theoretical compositions of $SrTiO_3(110)$ surface structures; Secs. S II and S III: XPS and XRD, respectively, of $SrTiO_3(110)$ homoepitaxial films; Sec. S IV: generalization of the approach to the determination of bulk nonstoichiometry of substrates and films.

[55] S. Gerhold, M. Riva, B. Yildiz, M. Schmid, and U. Diebold, Adjusting island density and morphology of the $SrTiO_3(110)$-(4×1) surface: Pulsed laser deposition combined with scanning tunneling microscopy, Surf. Sci. **651**, 76 (2016).

[56] M. Birkholtz, *Thin Film Analysis by X-Ray Scattering* (Wiley-VCH, Weinheim, 2005).

[57] Y. Kozuka, Y. Hikita, C. Bell, and H. Y. Hwang, Dramatic mobility enhancements in doped $SrTiO_3$ thin films by defect management, Appl. Phys. Lett. **97**, 012107 (2010).

[58] P. Ambwani, P. Xu, G. Haugstad, J. S. Jeong, R. Deng, K. A. Mkhoyan, B. Jalan, and C. Leighton, Defects, stoichiometry, and electronic transport in $SrTiO_{3-\delta}$ epilayers: A high pressure oxygen sputter deposition study, J. Appl. Phys. **120**, 055704 (2016).

[59] M. Choi, F. Oba, and I. Tanaka, Role of Ti Antisitelike Defects in $SrTiO_3$, Phys. Rev. Lett. **103**, 185502 (2009).

[60] J. H. Lee, G. Luo, I. C. Tung, S. H. Chang, Z. Luo, M. Malshe, M. Gadre, A. Bhattacharya, S. M. Nakhmanson, J. A. Eastman, H. Hong, J. Jellinek, D. Morgan, D. D. Fong, and J. W. Freeland, Dynamic layer rearrangement during growth of layered oxide films by molecular beam epitaxy, Nat. Mater. **13**, 879 (2014).

[61] T. Shi, Y. Chen, and X. Guo, Defect chemistry of alkaline earth metal (Sr/Ba) titanates, Prog. Mater. Sci. **80**, 77 (2016).

[62] S. M. Alay-e-Abbas, S. Nazir, S. Cottenier, and A. Shaukat, Evaluation of thermodynamics, formation energetics and electronic properties of vacancy defects in $CaZrO_3$, Sci. Rep. **7**, 8439 (2017).

[63] F. H. Taylor, J. Buckeridge, and C. R. A. Catlow, Defects and oxide ion migration in the solid oxide fuel cell cathode material $LaFeO_3$, Chem. Mater. **28**, 8210 (2016).

[64] Y.-L. Lee and D. Morgan, *Ab initio* and empirical defect modeling of $LaMnO_{3\pm\delta}$ for solid oxide fuel cell cathodes, Phys. Chem. Chem. Phys. **14**, 290 (2012).

[65] Z. Li, B. Liu, J. M. Wang, L. C. Sun, J. Y. Wang, Y. C. Zhou, and Z. J. Hu, First-principles study of point defects in stoichiometric and non-stoichiometric $Y_4Al_2O_9$, J. Mater. Sci. Technol. **29**, 1161 (2013).